Direct numerical simulations of turbulence subjected to a straining and destraining cycle

P. Gualtieri and C. Meneveau

Related Articles

Interactions between turbulence and flames in premixed reacting flows
Phys. Fluids 23, 125111 (2011)

Scaling of maximum probability density functions of velocity and temperature increments in turbulent systems
Phys. Fluids 23, 125101 (2011)

Development of a new dynamic procedure for the Clark model of the subgrid-scale scalar flux using the concept of optimal estimator
Phys. Fluids 23, 115103 (2011)

Lagrangian time correlations of vorticity alignments in isotropic turbulence: Observations and model predictions
Phys. Fluids 23, 101704 (2011)

Local and nonlocal pressure Hessian effects in real and synthetic fluid turbulence
Phys. Fluids 23, 095108 (2011)

Additional information on Phys. Fluids

Direct numerical simulations of turbulence subjected to a straining and destraining cycle

P. Gualtieri[1] and C. Meneveau[2]

[1]*Dipartimento di Meccanica e Aeronautica, Università di Roma La Sapienza, Via Eudossiana 18, 00184 Roma, Italy*
[2]*Department of Mechanical Engineering, Johns Hopkins University, 3400 N. Charles Street, Baltimore, Maryland 21218, USA*

In many turbulent flows, significant interactions between fluctuations and mean velocity gradients occur in nonequilibrium conditions, i.e., the turbulence does not have sufficient time to adjust to changes in the velocity gradients applied by the large scales. The simplest flow that retains such physics is the time dependent homogeneous strain flow. A detailed experimental study of initially isotropic turbulence subjected to a straining and destraining cycle was reported by Chen *et al.* ["Scale interactions of turbulence subjected to a straining-relaxation-destraining cycle," J. Fluid Mech. **562**, 123 (2006)]. Direct numerical simulation (DNS) of the experiment of Chen *et al.* ["Scale interactions of turbulence subjected to a straining-relaxation-destraining cycle," J. Fluid Mech. **562**, 123 (2006)] is undertaken, applying the measured straining and destraining cycle in the DNS. By necessity, the Reynolds number in the DNS is lower. The DNS study provides a complement to the experimental one including time evolution of small-scale gradients and pressure terms that could not be measured in the experiments. The turbulence response is characterized in terms of velocity variances, and similarities and differences between the experimental data and the DNS results are discussed. Most of the differences can be attributed to the response of the largest eddies, which, even if are subjected to the same straining cycle, evolve under different conditions in the simulations and experiment. To explore this issue, the time evolution of different initial conditions parametrized in terms of the integral scale is analyzed in computational domains with different aspect ratios. This systematic analysis is necessary to minimize artifacts due to unphysical confinement effects of the flow. The evolution of turbulent kinetic energy production predicted by DNS, in agreement with experimental data, provides a significant backscatter of kinetic energy during the destraining phase. This behavior is explained in terms of Reynolds stress anisotropy and nonequilibrium conditions. From the DNS, a substantial persistency of anisotropy is observed up to small scales, i.e., at the level of velocity gradients. Due to the time dependent deformation, we find that the major contribution in the Reynolds stresses budget is provided by the production term and by the pressure/strain correlation, resulting in large time variation of velocity intensities. The DNS data are compared with predictions from the classical Launder–Reece–Rodi isotropic production [B. E. Launder *et al.*, "Progress in the development of a Reynolds stress turbulence closure," J. Fluid Mech. **68**, 537 (1975)] Reynolds stress model, showing good agreement with some differences for the redistribution term. © *2010 American Institute of Physics*. [doi:10.1063/1.3453709]

I. INTRODUCTION

Many turbulent flows occur under nonequilibrium conditions, when the turbulence does not have sufficient time to adjust to changes in the velocity gradients, strains, rotation, as applied by the large scales or the mean flow. Examples include impinging turbulent boundary layers on propeller blades,[1] stagnation point flows, or the flow in the combustion chamber of reciprocating internal combustion engines.[2] Modeling scale interactions of turbulence in such scenario is challenging both for Reynolds averaged Navier–Stokes (RANS) and large eddy simulations (LESs), where many models assume some sort of equilibrium conditions[3–7] even though others include unsteady effects.[8–13]

Understanding turbulence that is out of equilibrium in the time domain is aided if the spatial structure of the flow can be simplified. Many basic topics in turbulence theory have been clarified in the idealized conditions of spatially homogeneous shear flows. For instance, fundamental issue of isotropy recovery at small scales has been successfully addressed both experimentally[14–17] and numerically.[18–20] Turbulence subjected to large-scale deformation has been considered in various papers since the seminal works of Batchelor[21] and Townsend.[22] The first data have been obtained in wind tunnel experiments, where properly designed distorting ducts were employed to achieve the desired large-scale deformation of spatially decaying turbulence.[23–27] From a theoretical point of view, rapid distortion theory (RDT) can be successfully employed whenever the characteristic time scale of the mean flow is much faster than the turbulent characteristic time scales (see, e.g., Refs. 28–32). Numerical experiments[33,34] have studied the response of turbulence to various types of straining flows. For instance, the

RDT calculation by Girimaji et al.[35] accounts for the effects of a rotating shear on velocity fluctuations, while the DNS of Yu et al.[36] analyzes the effects of a periodic shear.

Experimentally, the response of nearly steady isotropic fluctuations subjected to an irrotational two-dimensional (2D) axisymmetric strain was addressed in Refs. 37 and 38, while Chen et al.[39,40] analyzed the response of turbulence subjected to a straining-relaxation and destraining cycle. In this experiment, a planar strain was applied to isotropic turbulence in a water tank using a rapidly moving piston. Then a relaxation phase allowed the turbulence to begin relaxing toward isotropy, and then the deformation was reversed by pulling the piston back in a "destraining phase" of the cycle. 2D particle image velocimetry (PIV) was applied to measure velocities in a plane at various times during the cycle. However, the out of plane velocity was not available during the cycle, nor could pressure terms of velocity gradients at the viscous scale be evaluated to more fully characterize the turbulence during the cycle.

In the present paper, direct numerical simulation (DNS) reproducing the general conditions of the experiment of Chen et al.[39,40] are undertaken, but limited to smaller Reynolds number. We thus consider the response of initially isotropic turbulence subjected to a 2D time dependent strain flow as done experimentally by Chen et al.[40] Our aim is to complete the description of unsteady forced turbulence addressing complex observables, which are not amenable to experimental measurements. For instance, we can access the full velocity gradient tensor which allows a systematic reduction of the coherent vortical structures or characterizes the residual anisotropy at small scales. For modeling purposes, we also address the Reynolds stresses budget. In the strongly time dependent conditions we show that the production term is balanced only partially by the pressure/strain correlation, resulting in large time variation of velocity variances. While we also find that small scales are strongly anisotropic, the contribution of the pseudodissipation term in the budget is still negligible due to its much smaller magnitude compared to the other terms during the distortion. To shed more light into the various terms in the Reynolds stress budget, we compare the DNS data against the behavior of the pressure/strain term as predicted by a classical Reynolds stress transport model [in this case, we use the Launder–Reece–Rodi isotropic production (LRR-IP) model[41]].

This paper is organized as follows. In Sec. II, the formulation of Navier–Stokes equations for the homogeneous strain flow is discussed. Motivated by the comparison with experimental data by Chen et al.[40] reported in Sec. III, in Sec. IV, we present a detailed discussion of the role of the initial condition and the issues related to the confinement effects induced by the computational box. Sections V and VI report our major findings in terms of lack of isotropy recovery at small scales and Reynolds stresses budgets under nonequilibrium conditions. In Sec. VII, we summarize our conclusions.

II. HOMOGENEOUS STRAIN FLOW

We consider a turbulent flow in a confined box with an imposed mean velocity $\mathbf{U}(\mathbf{x},t)$. The total velocity $\mathbf{v}(\mathbf{x},t)$ is decomposed into its mean and fluctuation $\mathbf{u}(\mathbf{x},t)$, i.e., $\mathbf{v}=\mathbf{U}+\mathbf{u}$. The mean flow is given by a homogeneous time dependent, irrotational plane straining flow, i.e., $U_1(\mathbf{x},t)=a_1(t)x_1$; $U_2(\mathbf{x},t)=a_2(t)x_2$, subjected to $a_1(t)+a_2(t)=0$ due to incompressibility. The mean flow is in the plane (x_1,x_2), while x_3 is the spanwise coordinate. In making connections with the experiments (see Refs. 39 and 40), we will also denote x_1 as the horizontal coordinate and x_2 as the vertical coordinate.

The equations for the turbulent fluctuations follow from the decomposed Navier–Stokes equations, namely,

$$\nabla \cdot \mathbf{u} = 0,$$

$$\frac{\partial \mathbf{u}}{\partial t} + \mathbf{U} \cdot \nabla \mathbf{u} + \mathbf{u} \cdot \nabla \mathbf{U} = (\mathbf{u} \times \boldsymbol{\zeta}) - \nabla \Phi + \nu \nabla^2 \mathbf{u} + \mathbf{f}. \tag{1}$$

In Eq. (1), $\boldsymbol{\zeta}=\nabla \times \mathbf{u}$ is the fluctuating vorticity, $\Phi=p/\rho+u^2/2$ is the modified pressure, and $\mathbf{f}$ is an external isotropic forcing that we will discuss exhaustively in Sec. IV The divergence of the Reynolds stresses does not appear in Eq. (1) due to spatial homogeneity. The nonhomogeneous term $\mathbf{U}\cdot\nabla\mathbf{u}$ can be eliminated by using the transformation of variables proposed by Rogallo.[42] In the case of a planar 2D strain, the transformation of variables reads (see Ref. 33) as

$$\xi_1 = x_1 \exp[-f_1(t)],$$

$$\xi_2 = x_2 \exp[-f_2(t)], \tag{2}$$

$$\xi_3 = x_3,$$

where $f_i(t)=\int_0^t a_i(t')dt'$ is the total deformation. Using the transformation (2), the Navier–Stokes equations can be written in the deforming frame where the nonhomogeneous term is absorbed into the time derivative which transforms according to $\partial_t \rightarrow \partial_t - \mathbf{U}\cdot\nabla\mathbf{u}$. Therefore,

$$\nabla \cdot \mathbf{u} = 0,$$

$$\frac{\partial \mathbf{u}}{\partial t} + \mathbf{u} \cdot \nabla \mathbf{U} = (\mathbf{u} \times \boldsymbol{\zeta}) - \nabla \Phi + \nu \nabla^2 \mathbf{u} + \mathbf{f}. \tag{3}$$

In Eq. (3), the differential operators are defined in the transformed space by Eq. (2), namely, $\nabla=(\partial_{\xi_1}e^{-f_1}; \partial_{\xi_2}e^{-f_2}; \partial_{\xi_3})$. The differentiation includes time dependent metric factors which account for the deformation of the computational box in physical space. For instance, a domain of sides $\Lambda_1^0 \times \Lambda_2^0 \times \Lambda_3^0$ in physical space, after a time t, will be deformed into a box of edges $\Lambda_i(t)=\Lambda_i^0 e^{f_i(t)}$ (no summation over the index i is intended). Since the mean flow is irrotational, the computational box in physical space is stretched and squeezed without angular deformation. Equation (3) is now homogeneous in the fluctuations and highly accurate pseudospectral methods based on Fourier decomposition can be adopted for their numerical solution. In fact, in Fourier space, the divergence-free condition can be easily imposed by solving the Poisson equation for the modified pressure,

TABLE I. Summary of parameters of the various DNS. Runs $(2a)$–$(2e)$ refer to simulations with $k_f = 2$. The aspect ratio of the initial box is changed systematically for cases $(2a)$–$(2d)$. Case $(2d_h)$ has a higher Reynolds number. Results for run $(2e)$ have been averaged over 20 different initial conditions. Cases labeled $(5a)$–$(5d)$ are for forcing at $k_f = 5$, with computational boxes of different sizes. The last case, simulation $10(a)$, refers to a forcing at $k_f = 10$. The Taylor Reynolds number is defined as $\mathrm{Re}_\lambda = u_{\mathrm{rms}}\lambda/\nu$, where $u_{\mathrm{rms}} = (2/3k_0)^{1/2}$, $\lambda_0 = 10\nu k_0/\epsilon_0$, and $k_0 = \frac{1}{2}\langle u_i u_i \rangle$ denotes the turbulent kinetic energy.

Run	$\Lambda_1^0 \times \Lambda_2^0 \times \Lambda_3^0$	$N_1 \times N_2 \times N_3$	k_f	Re_{λ_0}	k_0	ϵ_0	L_0	η_0
$(2a)$	$2\pi \times 2\pi \times 2\pi$	$256 \times 48 \times 72$	2	35	1.49	0.97	0.95	0.038
$(2b)$	$2\pi \times 4\pi \times 2\pi$	$256 \times 96 \times 72$	2	33	1.33	0.91	0.91	0.038
$(2c)$	$2\pi \times 6\pi \times 2\pi$	$256 \times 144 \times 72$	2	33	1.44	1.03	0.88	0.038
$(2d)$	$2\pi \times 8\pi \times 2\pi$	$256 \times 192 \times 72$	2	40	1.52	1.00	0.93	0.037
$(2d_h)$	$2\pi \times 8\pi \times 2\pi$	$768 \times 576 \times 216$	2	80	1.39	0.82	0.71	0.011
$(2e)$	$2\pi \times 8\pi \times 2\pi$	$256 \times 192 \times 72$	2	40	1.45	0.98	0.91	0.037
$(5a)$	$2\pi \times 2\pi \times 2\pi$	$512 \times 96 \times 144$	5	33	0.90	1.00	0.40	0.019
$(5b)$	$2\pi \times 4\pi \times 2\pi$	$512 \times 192 \times 144$	5	33	0.90	0.98	0.39	0.019
$(5c)$	$\cdots$	$\cdots$	$\cdots$	$\cdots$	$\cdots$	$\cdots$	$\cdots$	$\cdots$
$(5d)$	$2\pi \times 8\pi \times 2\pi$	$512 \times 384 \times 144$	5	33	0.91	1.00	0.39	0.018
$(10a)$	$2\pi \times 2\pi \times 2\pi$	$1152 \times 216 \times 324$	10	40	0.64	1.00	0.20	0.008

$$\nabla^2\Phi = \nabla \cdot (\mathbf{h} + \mathbf{f}) - \nabla\mathbf{u}:\nabla\mathbf{U}^T - \nabla\mathbf{U}:\nabla\mathbf{u}^T, \qquad (4)$$

where we have defined the nonlinear term as $\mathbf{h} = \mathbf{u} \times \zeta$. Note that in Fourier space, wavenumbers depend on time (see Ref. 43) $\tilde{k}_{n_i}(t) = k_{n_i} e^{-f_i(t)}$, where $k_{n_i} = 2\pi n_i/\Lambda_i^0$, $n_i = -N_i/2, \ldots, N_i/2 - 1$ and N_i denotes the number of Fourier modes in the ith direction (see Table I for details). Time integration is performed by a low-storage fourth order explicit Runge–Kutta method, while the diffusive term is computed implicitly (see Ref. 44 for further details).

The initial conditions for the homogeneous strain simulations are provided by an ensemble of statistically steady turbulent fields obtained by forced DNS of homogeneous isotropic turbulence. Once initial conditions with targeted characteristics are achieved (see Sec. IV), the mean flow is switched on and the response of turbulent fluctuations to the imposed large-scale deformation is computed. The straining cycle is selected, specifying the mean velocity gradient $a(t) = a_1(t) = -a_2(t)$. In the simulations listed in Table I, the cycle has been chosen to match the experimental data of Chen *et al.*[40] In fact, the experimental data–displayed as symbols in Fig. 1—give the nondimensional strain rate $S^* = ak_0/\epsilon_0$ as a function of the nondimensional time $t^* = t\epsilon_0/k_0$. In these definitions, k_0 and ϵ_0 are the turbulent kinetic energy (tke) and the energy dissipation rate of the isotropic turbulence initial condition, respectively. The experimental data have been interpolated with piecewise polynomials—lines in Fig. 1—which are then used to evaluate the applied strain in the computational units of the simulations. Both k_0 and ϵ_0 are known from the initial condition and, for any time t, the strain in the DNS units is computed as $a(t) = S^* \epsilon_0/k_0$.

Before entering into more quantitative comparisons in Sec. III, we present in Fig. 2, some snapshots of the simulated coherent vortical structures along the cycle, providing a visual impression of the flow which might help the reader in appreciating latter discussions. This is for the simulation case $(2d_h)$ of Table I. The eduction criteria of the coherent struc-

tures are based on the velocity gradient tensor invariants Q and R,[45] combined in the discriminant $D = 27/4R^2 + Q^3$. This parameter provides good results when applied to flows characterized by intense mean velocity gradients.[46,47] We choose surfaces corresponding to the (positive) root-mean-square of D. Panels (a)–(c) of Fig. 2 show the vortical structures at three time instants during the straining phase. Initially, the flow is characterized by wormlike structures typical of isotropic turbulence. This is followed by stretching in the horizontal direction and contraction in the vertical one under the action of the applied strain. Consequently, the structures are tilted and aligned in the direction of the positive strain and vortex stretching is effective, resulting in large fluctuations in
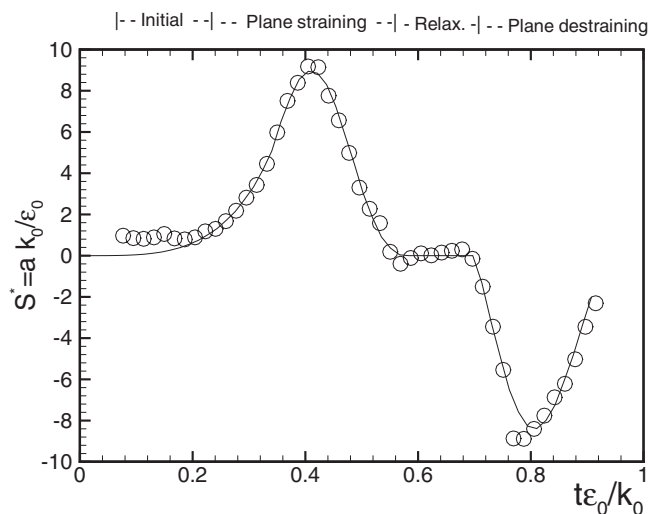

FIG. 1. Evolution of dimensionless strain rate $S^* = ak_0/\epsilon_0$ as a function of dimensionless time $t^* = t\epsilon_0/k_0$. Experimental data (symbols) have been interpolated using with sixth order piecewise polynomials (solid line). The straining cycle is characterized by four phases: initially isotropic during $0 < t^* < 0.24$; plane straining during $0.24 < t^* < 0.6$; relaxation phase $0.6 < t^* < 0.72$; and plane destraining phase during $0.72 < t^* < 0.92$. Data are made dimensionless with k_0 and ϵ_0, the turbulent kinetic energy and the energy dissipation rate of the turbulence during the initial condition, respectively.
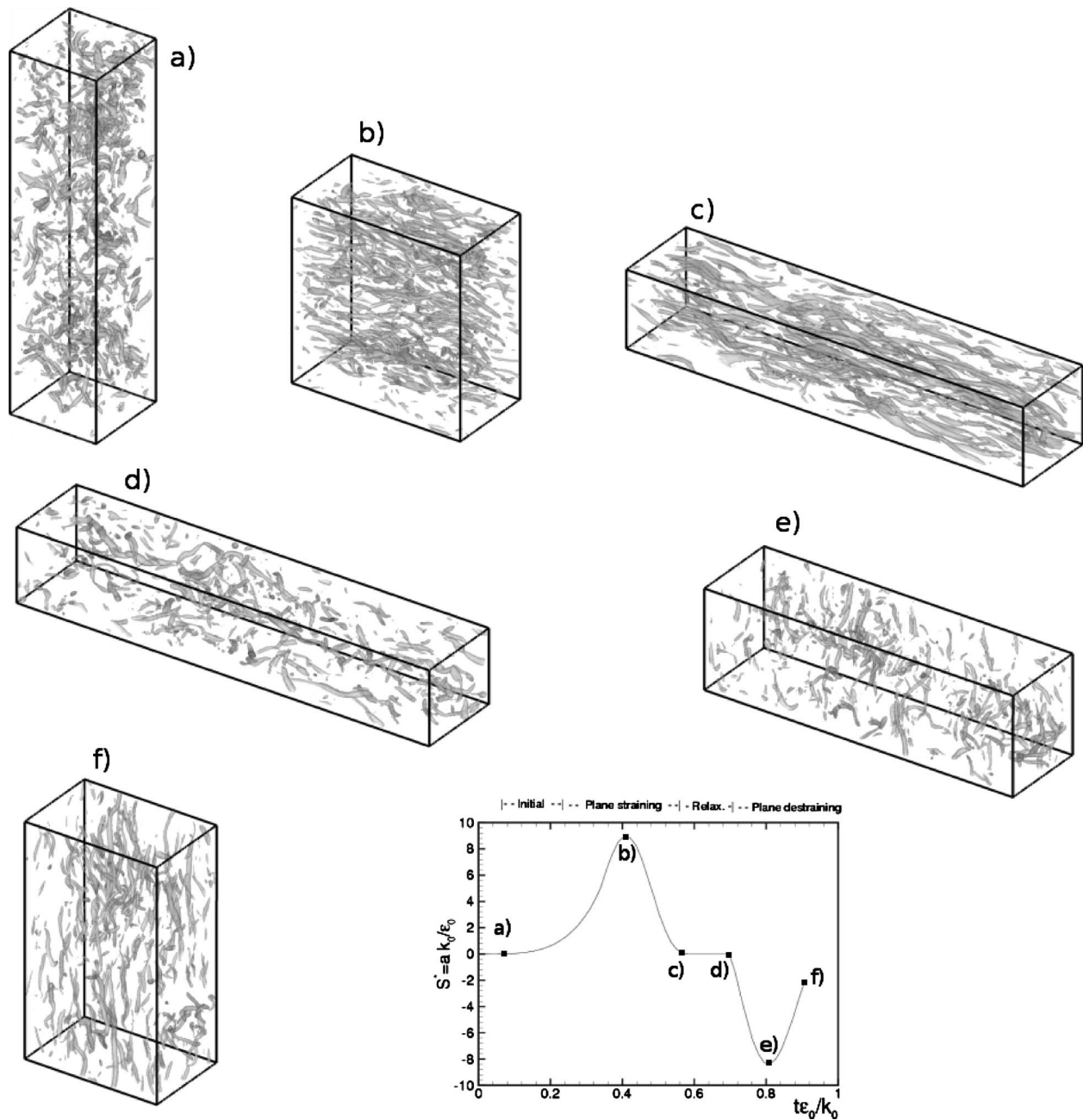
FIG. 2. Snapshots of the coherent vortical structures during the straining cycle visualized as isosurfaces of the invariant $D=27/4R^2+Q^3$. The invariants Q and R are the coefficients of the characteristic equation of the velocity gradient tensor. Isosurfaces of $D>0$ correspond to region where the local relative motion of two fluid particles is spiraling in a plane and are stretched in the orthogonal direction. In the snapshots isosurfaces corresponding to the value $D=\langle D^2\rangle^{1/2}$ are shown. From top to bottom and from left to right: initial isotropic state (a), peak of the applied straining (b), maximum deformation (c), end of the relaxation phase (d), peak of the negative straining (e), and end of the destraining phase (f). At the bottom right panel, the position of the snapshots during the straining cycle is indicated by black squares.

the vertical and spanwise velocity components (this will be examined in more detail later). At the end of the straining phase, turbulence is strongly anisotropic as revealed by the preferential alignment of vortical structures (and the large differences in the three velocity variances to be seen later). During the relaxation period, fluctuations are only stirred by the external forcing and isotropy recovery eventually takes place. Compare, for instance, panels (c) and (d) in Fig. 2 which correspond to the end of the straining phase and the end of the relaxation period, respectively. The signature of reisotropization is clear. The preferential alignment of the

coherent structures in the longitudinal direction is progressively lost and structures resemble much more the initial isotropic state even though, as we will discuss more quantitatively later, a fully isotropic state is not reached at the end of the relaxation phase. When the deformation is reversed during the destraining phase, the structures quickly align in the direction of the positive strain, see panels (e) and (f) of Fig. 2, where two snapshots corresponding to the peak of the negative strain and to the end of the destraining phase are shown, respectively. During the destraining phase, vortex stretching produces fluctuations in the horizontal velocity
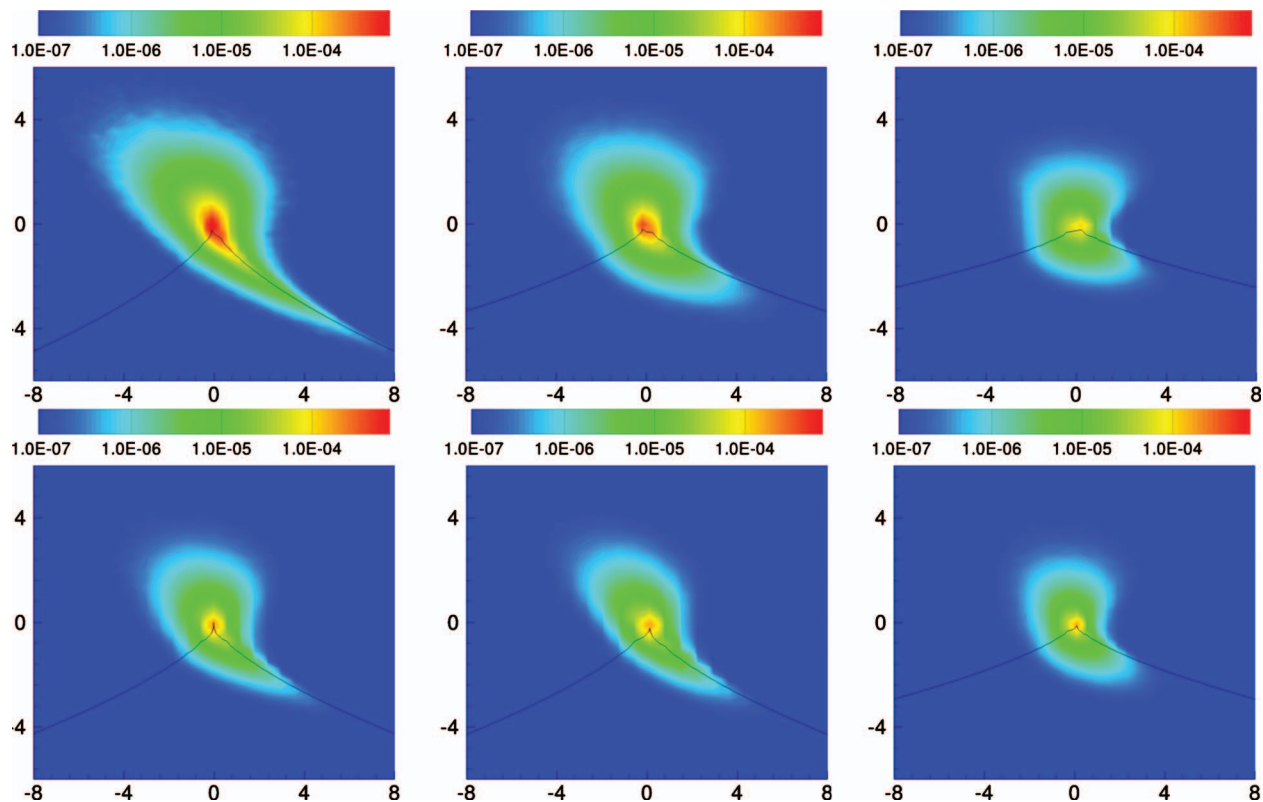
FIG. 3. (Color) Joint probability density function of the R-Q invariants of the velocity gradient tensor. The sample variables reported on the axis of the plots have been normalized with $\langle R^2 \rangle^{1/2}$ and $\langle Q^2 \rangle^{1/2}$, respectively. Time along the straining cycle is increasing from left to right and from top to bottom. Different panels correspond to the snapshots shown in Fig. 2. Top left initially isotropic turbulence, top center maximum strain intensity, top right end of the straining phase, bottom left end of the relaxation phase, bottom center maximum negative strain, and bottom right end of the destraining phase.

component in agreement with the observed growth of its variance, as discussed in Sec. III.

An alternative and more quantitative description of the small-scale structure of the velocity gradient tensor is provided by the joint probability distribution function (PDF) of the R-Q invariants[45–47] in Fig. 3. The events with $D>0$ and $R<0$ correspond to a locally stable spiraling motion, i.e., vortices. The half plane $D<0$ identifies strain-dominated motions, both unstable and stable $R \lessgtr 0$, respectively. Panels from left to right and from top to bottom in Fig. 3 correspond to the snapshots reported in Fig. 2. Initially, isotropic turbulence is characterized by the typical tear-drop shape of the joint PDF in the R-Q plane. Successively when fluctuations are subjected to the deformation imposed by the mean flow, the shape of the joint PDF is altered. During the straining phase, relatively more likely events occur in the unstable focus/stretching region (stable vortices) (see, for instance, the top right panel of Fig. 3 corresponding to the end of the straining phase). At the same time, the probability of events in the stable focus/stretching region and unstable node/saddle/saddle (vortex sheets) is reduced. After this stage, during the relaxation phase, the signature of isotropy recovery can be seen in the reappearance of the typical tear-drop shape (see bottom left panel of Fig. 3). Afterward, when the strain is reversed, the shape of the joint PDF is altered with the same trend discussed during the straining phase. Since the invariants R and Q are invariant under coordinate system

rotation, it makes sense that this description does not distinguish between effects of deformation in x_1 or x_2 directions.

III. COMPARISON WITH EXPERIMENTAL DATA

We begin with a presentation of the results of the most physically realistic simulation case, namely, case $(2d_h)$ of Table I, and a comparison against the experimental data of Chen *et al.*[40] The DNS is limited to moderate values of the Reynolds number, ranging from an initial value of $Re_{\lambda_0}=80$ to a maximum value of $Re_\lambda=130$ during the cycle. This is to be contrasted to the experimental Reynolds number $Re_\lambda=400$ of the initial condition in the experiment.

Figure 4 shows the energy spectra of the initial conditions normalized in Kolmogorov units [panel (a)] and large-scale units [panel (b)]. The symbols refer to the experimental data, while lines show the initial spectra of the various DNS that differ on how the forcing is applied. Different forcings are parametrized by the wavenumber k_f where its spectral density peaks [see Table I and Eq. (5)]. The details of these cases will be discussed later in Sec. IV A. An inertial-like range seems to develop only for the highest Reynolds number DNS data set, i.e., run $(2d_h)$, which is the case considered in the comparison. When the spectra are rescaled with Kolmogorov variables, as expected some collapse is observed in the high wavenumber range. Still, the experimental data did not show a decrease in the viscous range due to the
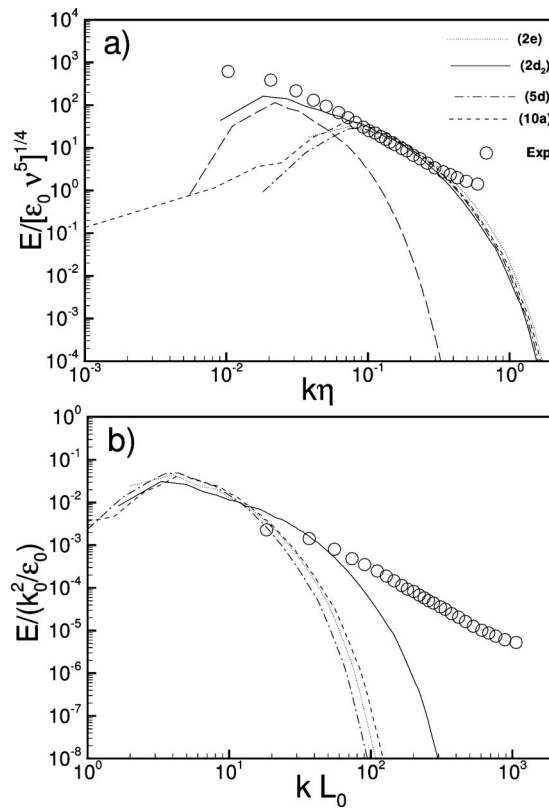
FIG. 4. Comparison of the energy spectra of initially isotropic turbulence. Experimental data (symbols). DNS data (lines) are reported for different cases: $(2e)$ dotted line, $(2d_h)$ solid line, $(5d)$ dashed-dotted line, and $(10a)$ dashed line (see Table I). (a) Energy spectra in Kolmogorov viscous units, the forcing power spectral density $\mathcal{F}$ is reported for case $(2d_h)$ (long dashed line). (b) Same data normalized with large-scale variables.
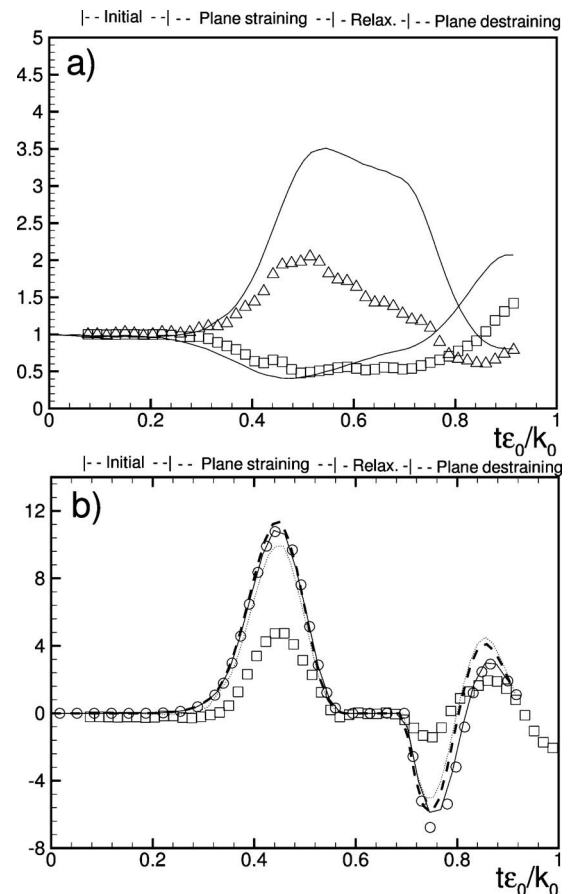

FIG. 5. (a) Comparison of the horizontal and vertical variances, normalized with their initial values. Experimental data, symbols: $\langle u_1^2 \rangle / \langle u_1^2 \rangle_0$ (squares) and $\langle u_2^2 \rangle / \langle u_2^2 \rangle_0$ (triangles). DNS data: $(2d_h)$ solid lines. (b) Turbulent kinetic energy production $\mathcal{P} = -a_1(t)\langle u_1^2 \rangle - a_2(t)\langle u_2^2 \rangle$ normalized with the dissipation rate of the initial condition ϵ_0. Experimental data (squares). DNS data: $(2e)$ (circles), $(2d_h)$ (solid line), $(5d)$ (dotted line), and $(10a)$ (heavy dashed line).

effects of experimental noise of the PIV at the largest resolved wavenumbers. When the data are made dimensionless in terms of the integral scale quantities, a collapse is not seen due essentially to inherent differences at the level of the largest energy containing scales of the flows. In the experimental setup, the initially statistically steady isotropic turbulence is realized in a water tank by means of spinning grids. As discussed by Chen *et al.*,[40] experimental data are available only for an intermediate range of scales since the largest scales are not spatially resolved in the finite size PIV measurement window. Also, at the largest scales the experiment is not expected to be completely isotropic due to confinement effects of the tank walls. See Ref. 40 for more details.

Even though the match of the two initial conditions is clearly incomplete, especially in the energy containing range, in Fig. 5(a) we compare the response of turbulence in terms of the horizontal and vertical velocity variances, normalized with corresponding values of the initial condition. Comparing experiments (symbols) and DNS (lines), the trends are seen to be similar. The amplitude of the variance in the horizontal direction is well reproduced until $t\epsilon_0/k_0 \sim 0.6$. The peak of $\langle u_1^2 \rangle$ and $\langle u_2^2 \rangle$ occurs at comparable times in the experiments and the DNS. During the relaxation period $\langle u_1^2 \rangle$ is almost constant in the experimental data, while it increases more rapidly in the DNS. This is due to a more intense redistribution of energy among the velocity components

given by the pressure/velocity correlation since the vertical component is more energetic in the DNS than in the experiments. As is evident, the amplitude for the vertical velocity component differs significantly, with peak variance of the DNS exceeding that of the experiment by almost a factor of 2, i.e., rms values differ by about 40%.

In Fig. 5(b), we compare the normalized turbulent kinetic energy production rate, $\mathcal{P} = -a_1(t)\langle u_1^2 \rangle - a_2(t)\langle u_2^2 \rangle$. As for the vertical velocity variance, the amplitude of the production is larger in the DNS when compared with experiments even though the position of the production peak is in good agreement. Notably, at the end of the relaxation phase, as soon as the mean flow is reversed, the DNS data show negative production, meaning that kinetic energy is transferred from the fluctuations to the mean flow (backscatter). This particular feature of nonequilibrium turbulence was also observed in the experimental data even if with a lower amplitude. In Fig. 6, a measure of the large-scale anisotropy of turbulent fluctuations is presented. To compare with the experimental data, a 2D surrogate of the Reynolds stresses deviatoric tensor is used, namely, $b_{11}^s = \langle u_1^2 \rangle / (\langle u_1^2 \rangle + \langle u_2^2 \rangle) - 1/2$. Note that this observable does not imply any normalization with the initial data and vanishes in a purely isotropic en-
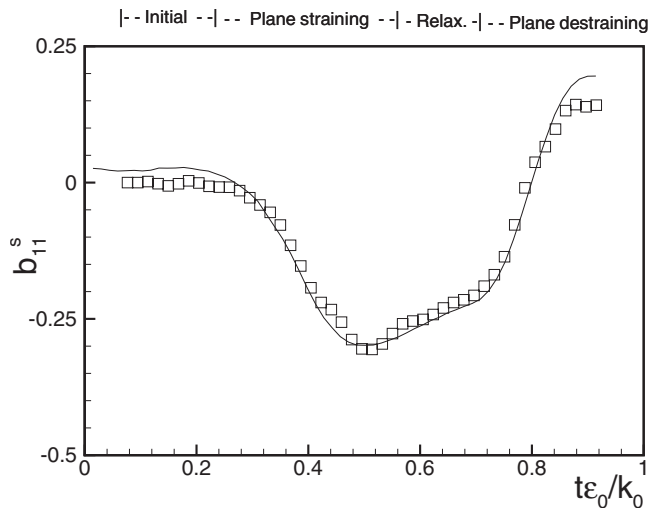
FIG. 6. 2D surrogate of the deviatoric Reynolds stresses tensor b_{11}^s (see text for the definition). Experimental data (squares) are compared with DNS data $(2d_h)$ (solid line).

semble. The agreement between DNS (lines) and the experiments (symbols) is very good, indicating that the degree of anisotropy is comparable between DNS and experiments when expressed in a dimensionless fashion.

Considering again the initial energy spectra normalized in terms of the tke k_0 and dissipation rate ϵ_0 (see Fig. 4), experimental and numerical data show a substantial difference. The energy containing range of the DNS is shifted toward the largest scales where corresponding experimental data are, unfortunately, not available. Since the response of turbulence in terms of velocity fluctuations and energy production is dominated by these scales, it is reasonable to expect substantial differences when comparing the two data sets. However, when we compute the Reynolds stresses deviatoric tensor, we are comparing the velocity variance of a single velocity component with the turbulent kinetic energy. This normalization measures a relative evolution of the velocity variances which is perhaps less dependent on the absolute position of the energy containing range.

The comparison between experimental and DNS data poses some important questions about the response of turbulence in a box, when an external large-scale deformation is imposed. In particular, the response of the largest eddies and possible confinement effects of the periodic computational box need to be examined in more detail. This is the subject of Sec. IV, before proceeding further to any physical analysis of the numerical data.

IV. INITIAL CONDITION AND CONFINEMENT EFFECTS

Motivated by the initial comparisons with experimental data in Sec. III, we now present a systematic analysis of finite size effects associated with the computational box. The box size can be compared with the integral scale of the turbulence in the initial condition. The latter is determined by the position of the applied forcing term **f**, which can be char-

acterized by its spectrum. Actually, the wavenumber k_f where the forcing spectrum peaks is expected to fix the integral scale of the resulting turbulence.

A. Forcing

The initial conditions for the homogeneous strain simulations are provided by companion DNS of homogeneous and isotropic turbulence. Statistically steady isotropic fields are obtained by an external random forcing term **f**, delta-correlated in time. We adopt the scheme described in Ref. 48. Unlike forcing in a few wavenumbers with fixed injection rate, or linear forcing scheme,[49,50] in the method of Ref. 48, the forcing is uncorrelated with the turbulent field. The energy injection rate can be controlled only by the forcing variance according to $\langle \mathbf{f} \cdot \mathbf{u} \rangle \propto \langle f^2 \rangle$ (see Ref. 48). With this type of forcing, the energy injection rate can be constant in time even during applied straining. The forcing is given in Fourier space by the coefficients $\widehat{f_i}(\mathbf{k},t) = f_i^0 \mathcal{F}^{1/2}(|\mathbf{k}|)\exp(\iota\theta)$, where f_i^0 is the amplitude selected to achieve the desired energy injection rate, θ is a random variable with uniform distribution in $[0, 2\pi]$, and $\mathcal{F}(|\mathbf{k}|)$ is the forcing spectral density given by

$$\mathcal{F}(|\mathbf{k}|) = \begin{cases} (k/k_f)^6 \exp[3(1-(k/k_f)^2)], & 0 < k < k_f \\ C_k k^{-5/3}, & k_f < k < k_1 \\ C_\eta \exp[-\beta(k-k_1)], & k > k_1. \end{cases} \quad (5)$$

In Eq. (5), the constants C_k and C_η are chosen to make the function $\mathcal{F}(|\mathbf{k}|)$ continuous at $k=k_f$ and $k=k_1$. The value k_f determines the position where the forcing has its peak, $k_1 = 1.5k_f$ and $\beta = 0.25$.

The initial energy spectra of velocity fluctuations achieved by means of Eq. (5) is shown in Fig. 4(a) for different values of k_f and Reynolds number. For comparison we have also plotted the forcing spectral density $\mathcal{F}$ for case $(2d_h)$.

Desired targeted initial conditions can be achieved by tuning the properties of the external forcing. In a statistically steady ensemble, the energy dissipation rate is controlled by the large-scale energy injection rate. In the simulation units, it is fixed approximately to $\epsilon_0 \simeq 1$. The initial value of the integral scale can be tuned by the forcing wavenumber k_f (see Table I for values achieved). Once ϵ_0 and k_f have been selected, the Taylor Reynolds number is fixed by the kinematic viscosity ν.

B. Finite-size computational domain effects

In this subsection, we address the finite size effects induced by the computational domain. We show that the response of turbulence to the imposed mean strain is greatly affected by the value of the initial integral scale in relation to the size and aspect ratio of the computational box. We discuss the various simulations reported in Table I, which differ for the position of the forcing wavenumber k_f, the aspect ratio of the box, and Reynolds number. The first lines of Table I refer to a set of simulations where the forcing wavenumber is fixed, $k_f=2$, and the aspect ratio of the box is systematically changed at fixed Reynolds number [cases
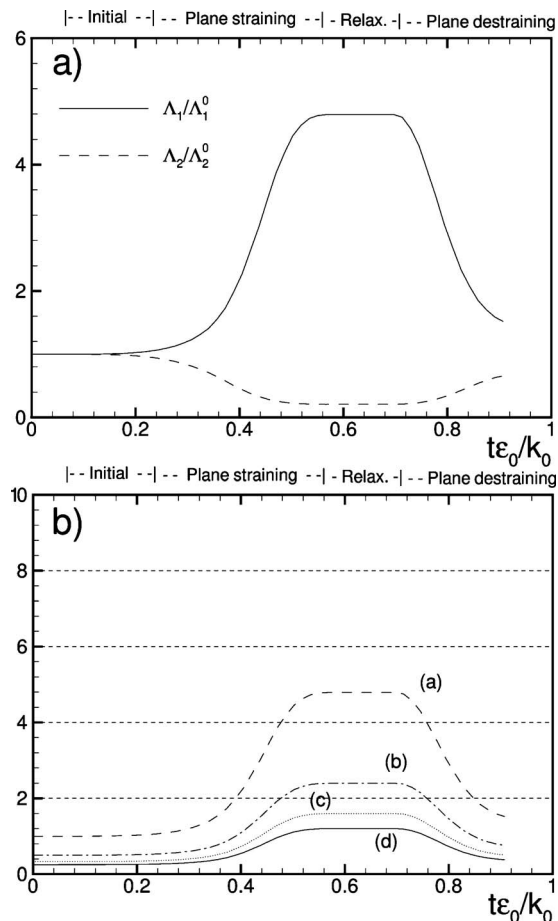
FIG. 7. (a) Deformation of the computational box in physical space during the straining cycle. The initial box is stretched by a factor of 5 in the horizontal direction (solid line), while it is compressed by the same ratio in the vertical direction (dashed line). (b) Time evolution of min $\tilde{k}_2(t)$ for four different aspect ratios of the computational. Dashed line $\Lambda_2^0 = 2\pi$, dashed-dotted line $\Lambda_2^0 = 4\pi$, dotted line $\Lambda_2^0 = 6\pi$, and solid line $\Lambda_2^0 = 8\pi$. Data progressively been labeled as $(a)-(d)$. The dimensions in the plane (x_1, x_3) are $\Lambda_1^0 \times \Lambda_3^0 = 2\pi \times 2\pi$ for all the simulations, see Table I.

FIG. 8. (a) Time evolution of the velocity variance in the horizontal direction $r_{11} = \langle u_1^2 \rangle / \langle u_1^2 \rangle_0$ for $k_f = 2$ and different aspect ratio of the initial box. From the smallest to the largest Λ_2^0, $(2a)$ (dashed line), $(2b)$ (dashed-dotted line), $(2c)$ (dotted line), and $(2d)$ (solid line). Data for case $(2e)$ (symbols) are also reported for comparison. Error bars are estimated by ensemble averaging on 20 different initial conditions. The amplitude of the error bar corresponds to $2\sigma/\sqrt{n}$, where $n = 20$ and σ is the variance. The error bars are on the order of the symbol size. (b) Same symbols as in the top panel. Data refer to the velocity variance in the vertical direction $r_{22} = \langle u_2^2 \rangle / \langle u_2^2 \rangle_0$.

$(2a)-(2d)]$. The data labeled $(2d_h)$ refer to $k_f = 2$ in the largest box and at a higher value of the Reynolds number using a large number of grid points. Case $(2e)$ has been run at a lower Reynolds number but for a large number of ensembles for better statistical convergence. This case is computed for an ensemble of 20 different initial conditions. This data set provides a measure of sensitivity to statistical convergence compared to the other simulations, where data from a single realization are presented. The next entries of Table I report a set of simulations where the forcing wavenumber has been shifted toward the smallest scales, i.e., $k_f = 5$ and $k_f = 10$ for runs $(5a)-(5d)$ and $(10a)$, keeping the Reynolds number constant. As a general comment, as the integral scale L_0 is progressively reduced, i.e., k_f is shifted toward the highest wavenumbers, the Kolmogorov scale $\eta_0 = (\nu^3 / \epsilon_0)^{1/4}$ becomes smaller. This, coupled with the need to still resolve the large scales of the flow at wavenumbers below k_f, explains the relatively high numerical resolution needed for our DNS even for a relatively small Reynolds number.

In Fig. 7(a), we show the time history of the horizontal $\Lambda_1(t)$ and vertical $\Lambda_2(t)$ computational box lengths during
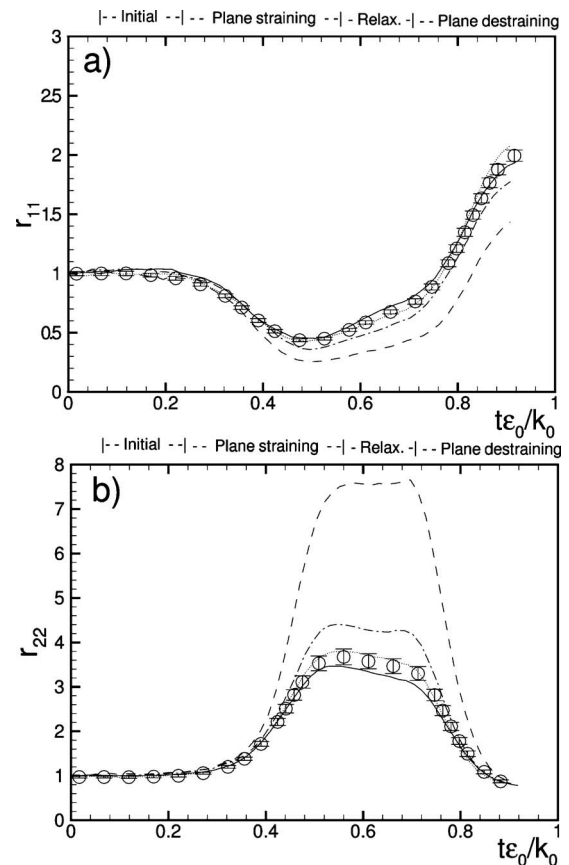
the straining cycle. Data are normalized with the corresponding values at $t = 0$. During the straining phase, the box is stretched by a factor of 5 in the horizontal direction and compressed by the same ratio in the vertical direction. During the destraining phase, the deformation is reversed almost completely. A rendering of the computational box in physical space has already been provided before in Fig. 2, where snapshots of the flow were visualized along the cycle. The same picture holds in Fourier space where the wavenumber in the vertical direction $\tilde{k}_2(t)$ first increased and then decreased, while the wavenumber in the horizontal direction $\tilde{k}_1(t)$ have an opposite behavior. In Fig. 7(b), we show min $\tilde{k}_2(t)$ during the cycle for the four different values of Λ_2^0 labeled $(a)-(d)$, respectively. In this plot the position of k_f during the cycle corresponds to a fixed horizontal line (the physical scale where the forcing is applied is fixed) that can be compared with min $\tilde{k}_2(t)$ for boxes with different aspect ratio.

The evolution of velocity variances $\langle u_1^2 \rangle$, $\langle u_2^2 \rangle$, and $\langle u_3^2 \rangle$ is shown in Figs. 8 and 9 for cases $(2a)-(2d)$ and $(2e)$. In such comparisons, the initial integral scale is fixed (i.e., all cases
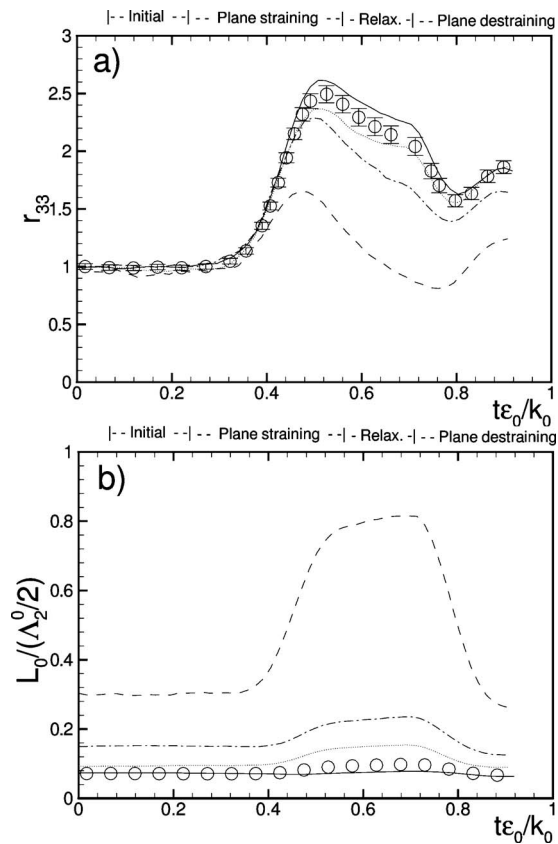
FIG. 9. (a) Time evolution of the velocity variance in the spanwise direction $r_{33} = \langle u_3^2 \rangle / \langle u_3^2 \rangle_0$ for $k_f = 2$ and different aspect ratio of the initial box. (b) Evolution of the integral scale normalized with the initial box length in the vertical direction $\Lambda_2^0/2$. Symbols and data as in Fig. 8.

have $k_f = 2$), while the aspect ratio of the computational box is changed systematically at fixed Reynolds number. Angular brackets denote spatial average and, for run (2e) also ensemble averaging over the time evolution of 20 different initial conditions. Results are normalized with the corresponding values at $t=0$ and are denoted by r_{11}, r_{22}, and r_{33}, respectively. During the initial phase, turbulence is in equilibrium with the external forcing, and it remains isotropic. During the straining phase, the variance $\langle u_1^2 \rangle$ decreases, while $\langle u_2^2 \rangle$ increases, in agreement with the fact that the principal axis of the Reynolds stress tensor is aligned with that of the mean deformation tensor when turbulence is initially isotropic. The response of the vertical velocity variance $\langle u_2^2 \rangle$ appears to be strongly dependent on the aspect ratio of the computational domain, as seen in Fig. 8(b). This suggests that there are considerable confinement effects due to the finite size of the computational box. In fact, during the cycle, the position of the most energetic mode is fixed by k_f, while the minimum wavenumber resolved in the vertical direction $\min \tilde{k}_y(t)$ grows [see Fig. 7(b)]. Therefore, k_f, i.e., the largest scales, may not be sufficiently resolved in the simulation for cases (2a) and (2b). Only the data set (2d) allows for an appropriate resolution of the largest modes. The same conclusions are achieved by considering the evolution of the spanwise velocity variance r_{33} in Fig. 9(a). It grows during the straining phase because of the energy redistribution

among velocity components due to the pressure/strain correlation $\langle w \partial_z p \rangle$. Note that the time evolution of the u_3 component was not measured in the experiments.

The sensitivity of turbulent fluctuations on the aspect ratio of the computational box can be also characterized in terms of the time evolution of the normalized integral scale [Fig. 9(b)]. Only when $k_f \gg \min \tilde{k}_y(t)$ along the entire cycle, one may expect that the integral scale will remain significantly smaller than the computational box size thus avoiding artificial confinement effects. For cases (2a)–(2c), the integral scale does not remain much smaller than the smallest dimension of the computational box, and therefore they are not very realistic at least at the largest scales of turbulence.

Our results show how a proper resolution of the largest scales of turbulent fluctuation is crucial in strained flows. The challenge of proper large-scale resolution of eddies also arises in the context of decaying isotropic turbulence.[51,52] During the decay, the largest scales of the flow grow continuously and eventually become on the order of the box size. It follows that the largest structures cannot be captured by the simulation and the onset of the self-similar behavior of turbulent fluctuations may be not correctly predicted, leading to a large scatter both of experimental and numerical data. Here, because of the more rapid change in large-eddy length scales, the challenges are even more pronounced.

Concerning the destraining phase, velocity variances are still anisotropic when the negative strain is applied after the relaxation phase. Under the effect of an opposite strain, the Reynolds stresses are first forced back to an isotropic state and then aligned again along the new principal directions as imposed by the mean flow. Actually, in the destraining phase, $\langle u_1^2 \rangle$ is always increasing, while $\langle u_2^2 \rangle$ decreases at a faster rate with respect to the relaxation phase. A different behavior is observed for $\langle u_3^2 \rangle$, which passes through a relative minimum.

Figures 10 and 11 present the results for all the other cases reported in Table I. In order to establish the sensitivity of the response to the Reynolds number, see results for case $(2d_h)$, and for the sensitivity to a shifting of the forcing toward higher wavenumbers, see results for cases (5a)–(5d) soon becomes independent of the aspect ratio of the box, since then the confinement constraint $\min \tilde{k}_y(t) \ll k_f$ is more easily satisfied. Actually, by doubling the initial box length in the vertical direction once [see run (5b)] and twice [see run (5d)], the response of the system does not change substantially as confirmed by a further shift of the forcing wavenumber up to $k_f = 10$ for run (10a). Note that all the simulations where confinement effects are absent are characterized by the similar response in terms of velocity variances and integral scale when rescaled with the forcing wavelength $\Lambda_f = 2\pi/k_f$ [see Fig. 11(b)]. For the most relevant cases, i.e., (2e), $(2d_h)$, (5d), and (10a), we show in Fig. 5(b) the tke production rate. In agreement with experimental data, at the beginning of the destraining phase, a negative value of turbulent kinetic energy production occurs due to a lack of isotropy recovery of the largest scales during the relaxation period. In these conditions turbulent kinetic energy goes from the fluctuations toward the mean flow, i.e., backscatter occurs. This observa-
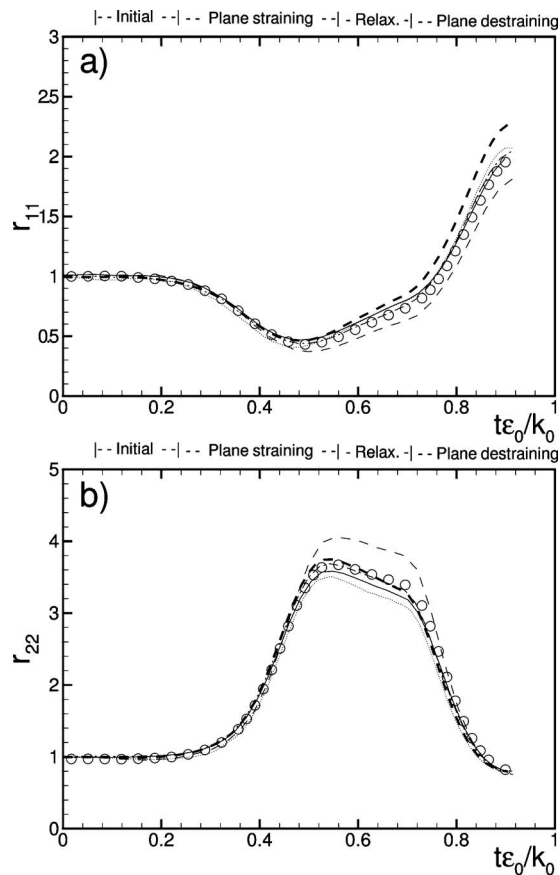
FIG. 10. (a) Time evolution of the velocity variance in the horizontal direction $r_{11} = \langle u_1^2 \rangle / \langle u_1^2 \rangle_0$ for $k_f = 2, 5, 10$ and different aspect ratio of the box. From the smallest to the largest Λ_2^0, $(2e)$ (symbols), $(2d_h)$ (dotted line) and $(5a)$ (dashed line), $(5b)$ (dashed-dotted line), $(5d)$ (solid line), and $(10a)$ (heavy dashed line). Data $(2e)$ (symbols) are reported to check statistical convergence, data set $(2d_h)$ provides sensitivity of the Reynolds number. (b) $r_{22} = \langle u_2^2 \rangle / \langle u_2^2 \rangle_0$. Same data and symbols as in the top panel.
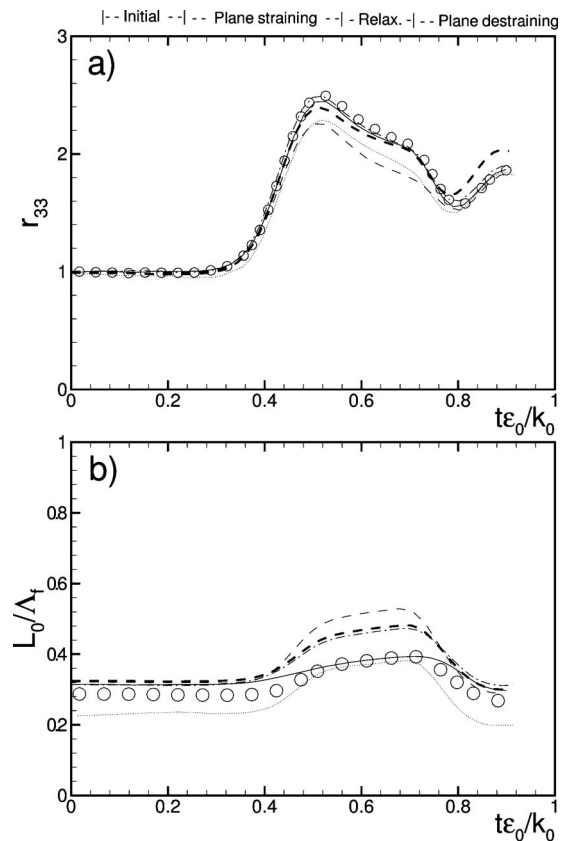

FIG. 11. Data as in Fig. 10. (a) Time evolution of the velocity variance in the spanwise direction $r_{33} = \langle u_3^2 \rangle / \langle u_3^2 \rangle_0$. (b) Normalized integral scale.

tion is independent of the parameter k_f once the largest scale of the flow are properly resolved, i.e., when confinement effects are avoided.

V. ANISOTROPY EVOLUTION AT LARGE AND SMALL SCALES

A fundamental paradigm in turbulence theory is small-scale isotropy being recovered through the orientational randomization associated with the inertial range energy transfer. Of course, in this case, the invariance under rotation of the Navier–Stokes equations is broken by the time dependent mean flow. In this section, we document anisotropy evolution at the large scales using the Reynolds stress tensor and at small scales using the pseudodissipation tensor.

At large scales, we focus on the deviatoric component of the Reynolds stresses tensor $b_{ij} = \langle u_i u_j \rangle / \langle u_k u_k \rangle - 1/3\, \delta_{ij}$. This indicator vanishes in a purely isotropic field where the three velocity variances are expected to be equal. Note that here we present results based on the three-dimensional data from the DNS and so we do not use 2D surrogates as had been done in Sec. III when comparing with experiments. The three nonvanishing components of the tensor b_{ij} are presented in Fig. 12(a). The cases differ in the forcing wavenumber k_f,

initial Reynolds number, and aspect ratio of the computational box. They all give almost the same results. Turbulence is initially isotropic and persists in this state until the production term becomes active during the straining phase, leading to strongly anisotropic fluctuations. During the relaxation phase, the production of turbulent kinetic energy due to the Reynolds stresses is inactive. Fluctuations are forced by the isotropic random forcing and are redistributed by the pressure-strain term. Hence, a relaxation toward a new isotropic state takes place.[53,54] However, the relaxation period $T_r = 0.15$ is too short when compared with the large-scale eddy turn over time $\tau = k/\epsilon \sim 1$ at the end of the straining phase. This means that there is only an incomplete isotropy recovery of the large scales. During the successive destraining phase turbulent fluctuations are first forced back to an isotropic state—note the transition in the slope of b_{ij} as soon as the destraining phase starts—which is achieved in correspondence of the negative peak of the strain (see Fig. 1). Successively, a new (reversed) anisotropic state is reached at the end of the destraining phase.

In a similar manner, small-scale anisotropy can be quantified by considering the deviatoric component of the pseudodissipation tensor $\epsilon_{ij} = 2\nu \langle \partial_k u_i \partial_k u_j \rangle$, i.e., by computing $d_{ij} = \epsilon_{ij} / \epsilon_{kk} - 1/3\, \delta_{ij}$, which is shown in Fig. 12(b). Considerations similar to those discussed for b_{ij} can be repeated. Initially, isotropic small scales are forced toward an anisotropic state during the straining phase. This means that the tke production mechanisms are effective also at small scales. Actu-
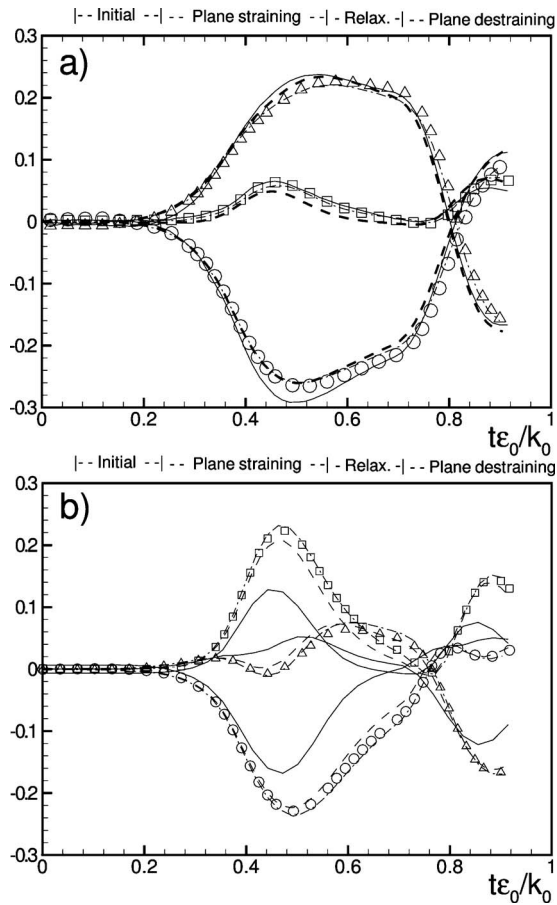
FIG. 12. (a) Large scale isotropy indicator $b_{ij} = \langle u_i u_j \rangle / \langle u_k u_k \rangle - 1/3\delta_{ij}$. Run 2$e$, b_{11} (circles), b_{22} (delta), and b_{33} (squares). For comparison case (2d_h) (solid line), (5d) (dashed-dotted line), and run (10a) (dashed line). (b) Small scale isotropy indicator $d_{ij} = \epsilon_{ij} / \epsilon_{kk} - 1/3\delta_{ij}$. Data and symbols as in the top panel.

ally, the anisotropy levels achieved by the velocity gradients are of the same order of magnitude compared to the degree of Reynolds stresses anisotropy [compare scales for panels (a) and (b) in Fig. 12].

During the successive relaxation phase, small scales evolve toward an isotropic state much quickly as compared to the largest ones. The Kolmogorov time is an estimate for the time needed for reisotropization at the small scales. In fact, at the end of the straining phase $\tau_\eta = 0.026$, which is significantly smaller when compared to $T_r = 0.15$. Finally, during the destraining phase, small scales are forced first toward an isotropic state to reach a new anisotropic configuration at the end of the cycle. In contrast to the values assumed by b_{33}, a large contribution to the small-scale anisotropy comes from the term d_{33} that characterizes the velocity gradients of the spanwise velocity in the vertical direction $\partial u_3 / \partial x_2$. This component is particularly active and related to the orientation of the vortical structures (see Fig. 2).

Finally, we observe that b_{ij} and d_{ij} can be expressed as structure functions evaluated at large and small scales, respectively. Considering the structure tensor $\langle \delta u_i \delta u_j \rangle$, where $\delta u_i = u_i(x+r) - u_i(x)$, in the limit of large scales $\langle \delta u_i \delta u_j \rangle_{r \to L_0} \to \langle u_i u_j \rangle$, while in the limit of small scales, e.g., $r \to \eta$ we have $\langle \delta u_i \delta u_j \rangle / |\mathbf{r}|^2 \to \epsilon_{ij}$. It follows that the isotropy recovery

is controlled by the scaling laws of the observable $\langle \delta u_i \delta u_j \rangle$ (see, e.g., Ref. 20). An in-depth study of this quantity as function of scale can be helpful in clarifying the process of small-scale isotropy recovery in the context of nonequilibrium turbulence and is relegated for a future study. Such an analysis can then be compared to results obtained in statistically steady homogeneous and nonhomogeneous anisotropic shear flows.[14,15,17,55,56] Our data can be used to extend such approaches to time dependent anisotropic flows (see, e.g., Ref. 57 in the context of decaying anisotropic turbulence).

VI. REYNOLDS STRESSES BUDGET

The dynamics of the time evolution of the variances in homogeneous unsteady flow can be analyzed by considering the balance equation for the Reynolds stresses. In homogeneous conditions it reduces to

$$\frac{\partial}{\partial t} \langle u_i u_j \rangle = \Pi_{ij} + \mathcal{P}_{ij} - \epsilon_{ij} + F_{ij}. \tag{6}$$

In Eq. (6), $\Pi_{ij} = -\langle p\partial_j u_i + p\partial_i u_j \rangle$ is the pressure/strain correlation, $\mathcal{P}_{ij} = -\langle u_i u_k \rangle \partial_k U_i - \langle u_j u_k \rangle \partial_k U_j$ is the production term, $\epsilon_{ij} = 2\nu \langle \partial_k u_i \partial_k u_j \rangle$ is the pseudodissipation tensor, and $F_{ij} = \langle f_i u_j \rangle + \langle f_j u_i \rangle$ is the forcing/velocity correlation (see, e.g., Ref. 3). The Reynolds stresses budget reduces to tke $k = \langle u^2 \rangle / 2$ equation when its trace is computed

$$\frac{\partial k}{\partial t} = \mathcal{P} - \epsilon + \mathcal{F}, \tag{7}$$

where $\mathcal{P} = -a_1(t)\langle u_1^2 \rangle - a_2(t)\langle u_2^2 \rangle$ is the tke production, $\epsilon = \nu \langle \partial_k u_i \partial_k u_i \rangle$ is energy dissipation rate, and $\mathcal{F} = \langle f_i u_i \rangle$ is the energy injection rate. The trace of the pressure/strain correlation Π_{ii} does not appear in this equation because of incompressibility. It is of interest to assess the role of the different terms in the budget of Eq. (6). Given the large-scale anisotropy of the turbulent fluctuations, the pressure/strain correlation is expected to be active in redistributing the energy among the three velocity components. Since our data indicate that residual anisotropy at small scales is comparable with the large scales (see Fig. 12), it is also interesting to assess the role of the pseudodissipation anisotropy in the budget.

The budget (6) is checked against the available DNS data in the left column of Fig. 13 where the three panels, labeled (a), (b), and (c) refer to the horizontal $\langle u_1^2 \rangle$, vertical $\langle u_2^2 \rangle$, and spanwise $\langle u_3^2 \rangle$ velocity components, respectively. Error bars computed for run (2e) are omitted in the plot for clarity since their amplitude $2\sigma / \sqrt{n}$ is on the order of the symbols size. The budget (6) is first checked by comparing the right hand side (RHS), i.e., RHS$_{ij} = \Pi_{ij} + \mathcal{P}_{ij} - \epsilon_{ij} + F_{ij}$ (diamonds in Fig. 13) with a direct measure of the unsteady term $\partial_t \langle u_i u_j \rangle$ (dashed line in Fig. 13). Excellent agreement can be seen.

Note the fluctuations of $\partial_t \langle u_i u_j \rangle$ around zero during the initial phase and the relaxation phase where turbulence is essentially statistically time independent. This is due to a lack of enough statistical samples. In any case, the budget (6) is well verified by our data. In fact, the direct measure of the
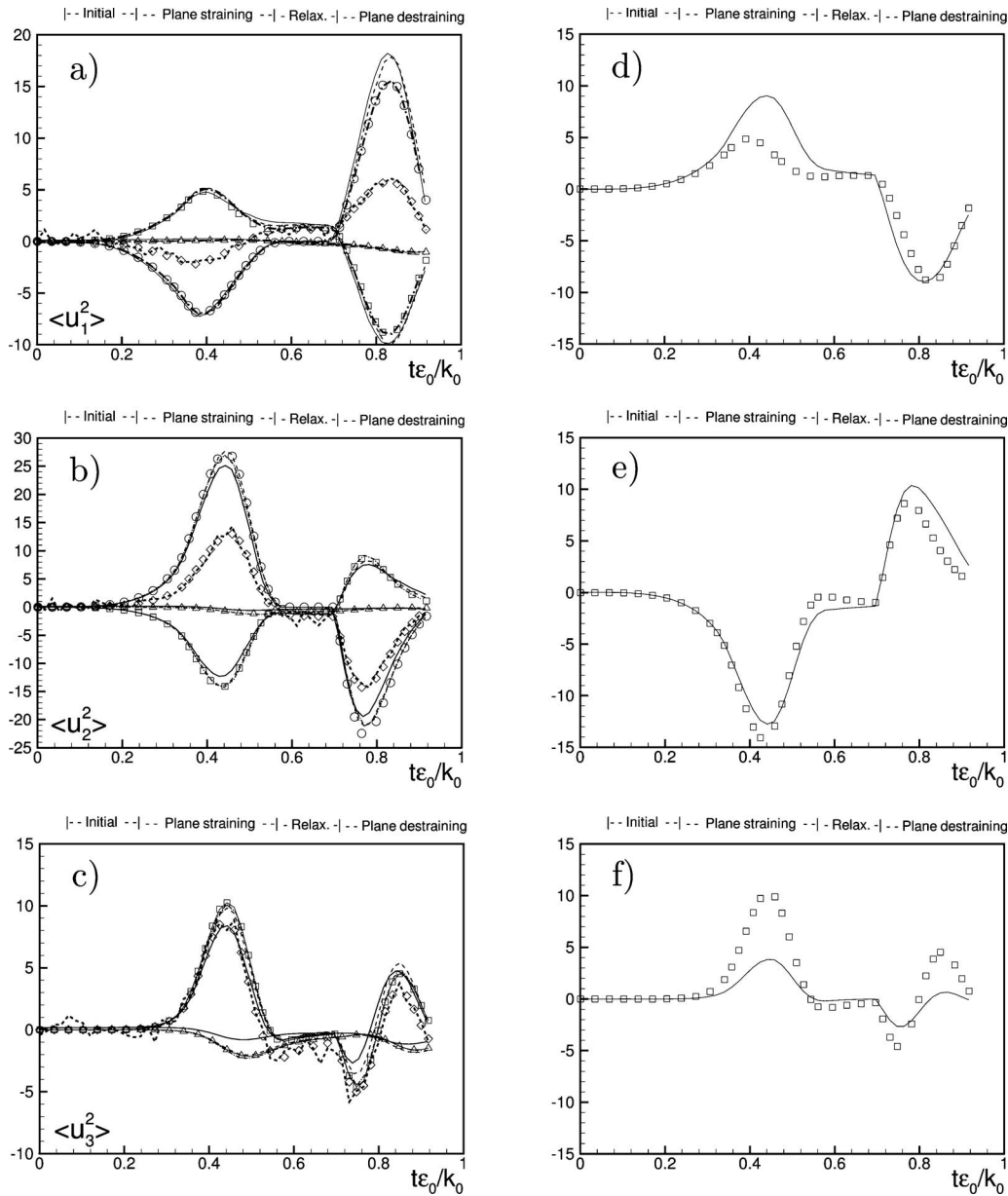
FIG. 13. [Panels (a)–(c)] Reynolds stresses budget [Eq. (6)] for run (2e) (symbols). Production $-a_i\langle u_i^2\rangle$ (circles), pressure/strain correlation $-2\langle u_i\partial_i p\rangle$ (squares), pseudodissipation, and forcing $-\epsilon_{ii}+\langle f_i u_i\rangle$ (triangles). No sun on the repeated index in all the terms. The RHS of Eq. (6) (diamonds) is compared against a direct measure of the unsteady term $\partial_t\langle u_i^2\rangle$ (dashed line). Cases (5d) (dashed-dotted line) and (10a) (dashed line) provide the sensitivity to k_f, run (2d_h) (solid line) to Re$_\lambda$. The error bars for case (2e) (not shown) are estimated as $2\sigma/\sqrt{n}$, where σ is the variance evaluated for the $n=20$ different initial conditions are of the order of the symbol size. [Panels (d)–(f)] The pressure/strain correlation (squares) is compared against the LRR-IP model (solid line) (Ref. 41).

unsteady term implies the evaluation of a time derivative that results noisy in the phases where the flow is not time dependent. However, during straining and destraining phases which are the most interesting for our purposes, the matching between RHS$_{ij}$ and $\partial_t\langle u_i u_j\rangle$ is clean. The comparison of the data set (2e) (symbols) with runs (5d) and (10a) (lines) provides the sensitivity to various forcing scales k_f, while run (2d_h) shows the effects of Reynolds number.

We discuss first the budget for the vertical velocity component $\langle u_2^2\rangle$ shown in Fig. 13, panel (b). During the straining phase the production $\mathcal{P}_{22}$ is positive, while the pressure/strain term Π_{22} acts as a sink which removes energy from the vertical component and redistributes it toward the other two

fluctuating velocity components. As we see from the plot, the production term $\mathcal{P}_{22}$ is about twice larger with respect to the pressure/strain term Π_{22}. Hence, the budget yields a positive $\partial_t\langle u_2^2\rangle$, leading to the growth of the vertical velocity variance during the straining phase. The dissipative and the forcing terms have been plotted together (triangles) and both are small when compared with the other terms in the budget. A similar behavior is observed during the destraining phase where the production term $\mathcal{P}_{22}$ is now negative and the pressure term Π_{22} acts as a source term. Now the budget yields a negative $\partial_t\langle u_2^2\rangle$, resulting in a depletion of the vertical velocity variance.

Similar features are observed for the horizontal velocity

component. Here, the role of production and pressure/strain correlation is exchanged along the cycle. During the straining phase the production term $\mathcal{P}_{11}$ is negative, while the pressure term Π_{11} acts as a source for fluctuations, thus requiring $\partial_t \langle u_1^2 \rangle$ to be negative. Successively, during the relaxation phase, $\Pi_{11} > 0$ since pressure is redistributing energy among the velocity components resulting in an increase of the horizontal velocity variance, $\partial_t \langle u_1^2 \rangle \simeq \Pi_{11} > 0$, in agreement with the reisotropization occurring during this phase. Finally, during destraining the production term is positive and the pressure term acts as a sink. The budget is again balanced by a positive unsteady term. Both dissipation and forcing give a negligible contribution.

The budget for the spanwise variance $\langle u_3^2 \rangle$ shown in panel (c) differs from the previous two because the production term is absent. Hence, the balance is essentially between the pressure/strain correlation Π_{33} and the unsteady term $\partial_t \langle u_3^2 \rangle$. The relative contribution of dissipation and forcing can now be appreciated more during some phases of the cycle. Π_{33} is a source for fluctuations during the straining phase, while at the end of the relaxation phase, it acts first as a sink and then as a source again. The behavior of Π_{33} resembles the turbulent kinetic energy production term $\mathcal{P}$ shown in Fig. 5. At the end of the relaxation period, both $\partial_t \langle u_1^2 \rangle$ and $\partial_t \langle u_2^2 \rangle$ are small when compared with the other terms in the budget. It follows that $0 \simeq \Pi_{11} + \mathcal{P}_{11}$ and $0 \simeq \Pi_{22} + \mathcal{P}_{22}$, hence $\partial_t \langle u_3^2 \rangle \simeq \Pi_{33} = -(\Pi_{11} + \Pi_{22}) \simeq \mathcal{P}_{11} + \mathcal{P}_{22} = \mathcal{P} < 0$.

As a final note, we comment on the dissipation anisotropy and its relative irrelevance in the budget. In Sec. V, we have shown how the dimensionless anisotropy at small scales was large and of the same order of the large-scale anisotropy directly induced by the mean flow on velocity fluctuations (see Fig. 12). However, the role the pseudodissipation tensor in the Reynolds stresses budget is very small. This is due to the fact that the applied straining generates production that dwarfes the molecular dissipation rate. Therefore, even if the dissipation tensor is relatively highly anisotropic, its magnitude is still small compared to production, the pressure/strain correlation, and the unsteady term.

To conclude this section, we use the data as a benchmark for a classic Reynolds stress closure model, while an exhaustive comparison with different models is out of the scope of this paper. We consider the classical LRR-IP model by Lauder *et al.*[41] and we compare the pressure/strain correlation against its "*a priori*" estimate. In the right column of Fig. 13, we have plotted the pressure/strain term as directly measured from the DNS data for case (2*e*) (squares). Panels from top to bottom refer to the three velocity components, respectively. The solid line in the panels gives the estimate provided by the LRR-IP model

$$\Pi_{ij}^{\text{mod}} = -C_R \frac{k}{\epsilon}\left(\langle u_i u_j \rangle - \frac{2}{3}k\delta_{ij}\right) - C_2\left(\mathcal{P}_{ij} - \frac{2}{3}\mathcal{P}\delta_{ij}\right), \quad (8)$$

with $C_R = 1.8$, $C_2 = 3/5$, and $\mathcal{P} = \mathcal{P}_{kk}/2$ (as taken from Ref. 3). It is an *a priori* comparison because we use the measured Reynolds stress and production terms to evaluate the RHS of Eq. (8) for the model.

In the model the first term on the RHS accounts for the return to isotropy of initially anisotropic turbulence, while the second is the so called isotropization of production, i.e., it accounts for the effect of pressure/strain term in redistributing energy among the velocity components when initially isotropic turbulence is subjected to anisotropic production. Both these features are present in our flow. In fact, during the straining phase, initially isotropic turbulence is subjected to anisotropic production, while isotropy recovery occurs during the relaxation phase. The qualitative behavior of the pressure/strain term is captured well by the model (see the right column of Fig. 13). However, the amplitude of the redistribution is predicted well only for the vertical velocity component [panel (e)]. Concerning the horizontal component shown in panel (d), the model overpredicts the pressure/strain term during the straining phase, while it gives reasonable results during the relaxation and destraining phases. In panel (f), we show the comparison for the spanwise component, which is the least accurate prediction.

VII. FINAL REMARKS

The response of homogeneous turbulence subjected to a straining and destraining cycle has been studied using DNS. One goal has been to supplement the experiments of Chen *et al.*,[40] who measured turbulence during such a cycle experimentally. The DNS has been analyzed using several one-point observables such as velocity variances, large- and small-scale anisotropy indicators, turbulent kinetic energy production rates, and the various terms in the Reynolds stresses budget equation.

Particular attention has been placed in identifying appropriate forcing scales with respect to the computational box size and aspect ratio. In particular, we have shown that confinement effects occur whenever the largest scales of the flow are poorly resolved in the simulation. Whenever $k_f \simeq \min \widetilde{k}_y(t)$ during the straining cycle, the response of turbulence is noticeably affected by confinement effects and depends on the aspect ratio of the box. On the contrary, when largest scales are well resolved during the entire cycle, i.e., when the integral scale is always considerably smaller, the smallest dimension of the computational box, the response of turbulence is free from artificial confinement effects and is independent of the position of the random forcing, i.e., independent of the parameter k_f.

Numerical results are compared against the experimental findings of Chen *et al.*[40] Velocity variances present the same qualitative behavior as found experimentally even though the amplitude of the response is larger in the DNS simulations, in the contracting direction in which the variances grow the most. This difference has been explained in terms of a substantial mismatch between experiments and simulations at the largest scales. Quantities that are nondimensionalized using time-evolving quantities, such as the Reynolds stresses anisotropy tensor, show very good agreement between simulation and experiments.

The lack of isotropy recovery of the largest scales at the end of the relaxation phase leads to a negative value of the turbulent kinetic energy production rate when the strain is

reversed. This behavior, as already observed experimentally, results in a backscatter of turbulent kinetic energy from the fluctuations to the mean flow. Probing the DNS further, it is shown that small scales reach levels of anisotropy comparable with those of the largest scales during the most strained phases of the cycle. It follows that in nonequilibrium conditions, a significant range of scales is affected by the anisotropic mechanisms of turbulent kinetic energy production.

The budget of the Reynolds stresses has been studied during the entire cycle to better understand the role of the pressure/strain correlation during nonequilibrium conditions. This term redistributes energy among the different velocity components. We find that the production term is only partially balanced by the pressure/strain correlation. Since the dissipation tensor turns out to have only minor contributions during straining or destraining, the rate of change is large, consistent with the observed large variation of the velocity variances during the cycle.

Finally, we have compared the predictions of the classical LRR-IP model with the measurements. Qualitatively, the agreement is good, but leaves much to be desired in predicting the correct amplitudes of the pressure-strain correlation term for two out of the three components of variance. Further studies of the scale-dependence response of stresses and comparisons with more RANS and LES models could provide further understanding of this nonequilibrium turbulent flow.

ACKNOWLEDGMENTS

[1] M. Sinha, J. Katz, and C. Meneveau, "Quantitative visualization of the flow in a centrifugal pump with diffuser vanes-ii addressing passage-average and large eddy simulation modeling issues in turbomachinery flows," J. Turbomach. **122**, 108 (2000).

[2] D. C. Haworth and K. Jansen, "Large eddy simulation on unstructured deforming meshes: Towards reciprocationg IC engines," Comput. Fluids **29**, 493 (2000).

[3] S. B. Pope, *Turbulent Flows* (Cambridge University Press, Cambridge, UK, 2000).

[4] C. Meneveau and J. Katz, "Scale-invariance and turbulence models for large eddy simulation," Annu. Rev. Fluid Mech. **32**, 1 (2000).

[5] C. Cambon and J. F. Scott, "Linear and non linear models of anisotropic turbulence," Annu. Rev. Fluid Mech. **31**, 1 (1999).

[6] C. G. Speziale, S. Sarkar, and T. B. Gatski, "Modelling pressure strain correlation of turbulence: An invariant dynamical systems approach," J. Fluid Mech. **227**, 245 (1991).

[7] C. G. Speziale, T. B. Gatski, and S. Sarkar, "On testing models for the pressure strain correlation of turbulence using direct simulations," Phys. Fluids A **4**, 2887 (1992).

[8] S. S. Girimaji, "Pressure strain correlation modeling of complex turbulent flows," J. Fluid Mech. **422**, 91 (2000).

[9] I. Hadžić, K. Hanjalić, and D. Laurence, "Modeling the response of turbulence subjected to cyclic irrotational strain," Phys. Fluids **13**, 1739 (2001).

[10] P. E. Hamlington and W. J. A. Dahm, "Reynolds stress closure for non-equilibrium effects in turbulent flows," Phys. Fluids **20**, 115101 (2008).

[11] P. E. Hamlington and W. J. A. Dahm, "Frequency response of periodically sheared homogeneous turbulence," Phys. Fluids **21**, 055107 (2009).

[12] W. J. T. Bos, T. T. Clark, and R. Rubinstein, "Small scale response and modeling of periodically forced turbulence," Phys. Fluids **19**, 055107 (2007).

[13] B. A. Pettersson-Reif, T. B. Gatski, and C. L. Rumsey, "On the behavior of two-equation models in nonequilibrium homogeneous turbulence," Phys. Fluids **18**, 065109 (2006).

[14] B. Jacob, C. M. Casciola, A. Talamelli, and E. Alfredsson, "Scaling of mixed structure functions in turbulent boundary layer," Phys. Fluids **20**, 045101 (2008).

[15] B. Jacob, C. M. Casciola, G. Iuso, and L. Biferale, "Anisotropic fluctuations in turbulent shear flows," Phys. Fluids **16**, 4135 (2004).

[16] X. Shen and Z. Warhaft, "The anisotropy of small scale structures in high Reynolds number ($\text{Re}_\lambda \sim 1000$) turbulent shear flow," Phys. Fluids **12**, 2976 (2000).

[17] Z. Warhaft and X. Shen, "On higher order mixed structure functions in laboratory shear flow," Phys. Fluids **14**, 2432 (2002).

[18] J. Schumacher, "Derivative moments in stationary homogeneous turbulent shear turbulence," J. Fluid Mech. **441**, 109 (2001).

[19] J. Schumacher, K. R. Sreenivasan, and P. K. Yeung, "Derivative moments in turbulent shear flows," Phys. Fluids **15**, 84 (2003).

[20] C. M. Casciola, P. Gualtieri, B. Jacob, and R. Piva, "The residual anisotropy of small scales in high shear turbulence," Phys. Fluids **19**, 101704 (2007).

[21] G. K. Batchelor and I. Proudman, "The effect of rapid distortion of a fluid in turbulence," Q. J. Mech. Appl. Math. **7**, 83 (1954).

[22] A. A. Townsend, "The uniform distortion of homogeneous turbulence," Q. J. Mech. Appl. Math. **7**, 104 (1954).

[23] H. J. Tucker and A. J. Reynolds, "The distortion of turbulence by irrotational plane strain," J. Fluid Mech. **32**, 657 (1968).

[24] J. F. Keffer, "The uniform distortion of a turbulent wake," J. Fluid Mech. **22**, 135 (1965).

[25] A. J. Reynolds and H. J. Tucker, "The distortion of turbulence by general uniform irrotational plane," J. Fluid Mech. **68**, 673 (1975).

[26] J. N. Gence and J. Mathieu, "The return to isotropy of an homogeneous turbulence having been submitted to two successive plane strains," J. Fluid Mech. **101**, 555 (1980).

[27] J. N. Gence and J. Mathieu, "On the application of successive plane strains to grid generated turbulence," J. Fluid Mech. **93**, 501 (1979).

[28] M. J. Lee, "Distortion of homogeneous turbulence by axisymmetric strain and dilatation," Phys. Fluids A **1**, 1541 (1989).

[29] J. R. C. Hunt and D. J. Carruthers, "Rapid distortion theory and the problems of turbulence," J. Fluid Mech. **212**, 497 (1990).

[30] K. Mahesh, S. K. Lele, and P. Moin, "The response of anisotropic turbulence to rapid homogeneous one-dimensional compression," Phys. Fluids **6**, 1052 (1994).

[31] N. K.-R. Kevlahan and J. R. C. Hunt, "Nonlinear interactions in turbulence with strong irrotational straining," J. Fluid Mech. **337**, 333 (1997).

[32] P. Sagaut and C. Cambon, *Homogeneous Turbulence Dynamics* (Cambridge University Press, Cambridge, UK, 2008).

[33] M. Lee and W. Reynolds, "Numerical experiments on the structure of homogeneous turbulence," Stanford University Report No. TF-24, 1985.

[34] S. S. Girimaji, E. Jeong, and S. V. Poroseva, "Pressure strain correlation in homogeneous anisotropic turbulence subjected to rapid strain dominated distortion," Phys. Fluids **15**, 3209 (2003).

[35] S. S. Girimaji, J. R. O'Neil, and D. Yu, "Rapid distortion analysis of homogeneous turbulence subjected to rotating shear," Phys. Fluids **18**, 085102 (2006).

[36] D. Yu and S. S. Girimaji, "Direct numerical simulations of homogeneous turbulence subjected to periodic shear," J. Fluid Mech. **566**, 117 (2006).

[37] S. Liu, J. Katz, and C. Meneveau, "Evolution and modeling of subgrid scales during rapid straining of turbulence," J. Fluid Mech. **387**, 281 (1999).

[38] S. Ayyalasomayajula and Z. Warhaft, "Nonlinear interactions in strained axisymmetric high Reynolds number turbulence," J. Fluid Mech. **566**, 273 (2006).

[39] J. Chen, J. Katz, and C. Meneveau, "Implication of mismatch between stress and strain-rate in turbulence subjected to rapid straining and de-

straining on dynamic les models," ASME J. Fluids Eng. **127**, 840 (2005).

[40] J. Chen, C. Meneveau, and J. Katz, "Scale interactions of turbulence subjected to a straining-relaxation-destraining cycle," J. Fluid Mech. **562**, 123 (2006).

[41] B. E. Launder, G. J. Reece, and W. Rodi, "Progress in the development of a Reynolds stress turbulence closure," J. Fluid Mech. **68**, 537 (1975).

[42] R. S. Rogallo, "Numerical experiments in homogeneous turbulence," NASA Technical Report No. T-M 81315, 1981.

[43] A. A. Townsend, *The Structure of Turbulent Shear Flow* (Cambridge University Press, Cambridge, UK, 1956).

[44] P. Gualtieri, C. M. Casciola, R. Benzi, G. Amati, and R. Piva, "Scaling laws and intermittency in homogeneous shear flow," Phys. Fluids **14**, 583 (2002).

[45] M. S. Chong, A. E. Perry, and B. J. Cantwell, "A general classification of three-dimensional flow fields," Phys. Fluids. A **2**, 765 (1990).

[46] H. M. Blackburn, N. N. Mansour, and B. J. Cantwell, "Topology of fine scale motions in turbulent channel flow," J. Fluid Mech. **310**, 269 (1996).

[47] M. S. Chong, J. Soria, A. E. Perry, J. Chacin, B. J. Cantwell, and Y. Na, "Turbulence structures of wall bounded shear flows found using DNS data," J. Fluid Mech. **357**, 225 (1998).

[48] K. Alvelius, "Random forcing of three-dimensional homogeneous turbulence," Phys. Fluids **11**, 1880 (1999).

[49] T. S. Lundgren, "Linearly forced turbulence," in *Center for Turbulence Research Annual Research Briefs 2003* (Center for Turbulence Research, Stanford, CA, 2003), p. 461.

[50] C. Rosales and C. Meneveau, "A minimal multiscale Lagrangian map to synthesize non-Gaussian turbulent vector fields," Phys. Fluids **18**, 075104 (2006).

[51] S. M. de Bruyn Kops and J. Riley, "Direct numerical simulation of laboratory experiments in isotropic turbulence," Phys. Fluids **10**, 2125 (1998).

[52] H. Wang and W. K. George, "The integral scale in homogeneous isotropic turbulence," J. Fluid Mech. **459**, 429 (2002).

[53] K. Choi and J. L. Lumley, "The return to isotropy of homogeneous turbulence," J. Fluid Mech. **436**, 59 (2001).

[54] S. Sarkar and C. G. Speziale, "A simple nonlinear model for the return to isotropy in turbulence," Phys. Fluids A **2**, 84 (1990).

[55] S. G. Saddoughi and S. V. Veeravalli, "Local isotropy in turbulent boundary layer at high Reynolds number," J. Fluid Mech. **268**, 333 (1994).

[56] R. A. Antonia, L. Djenidi, and P. R. Spalart, "Anisotropy of the dissipation tensor in a turbulent boundary layer," Phys. Fluids **6**, 2475 (1994).

[57] L. Biferale, G. Boffetta, A. Celani, A. Lanotte, F. Toschi, and M. Vergassola, "The decay of homogeneous anisotropic turbulence," Phys. Fluids **15**, 2105 (2003).